

Energy eigenstates of electrons, magnons, and phonons in Fe_3O_4 (magnetite), MnFe_2O_4 (jacobsite), and mixed Mn–Zn ferrite

Deepak Dhariwal^{*1}, Michael R. von Spakovsky², and William T. Reynolds Jr.¹

¹Department of Materials Science and Engineering, Virginia Tech, USA 24060

²Department of Mechanical Engineering, Virginia Tech, USA 24060

^{*}Email: deepak20@vt.edu

Abstract

We report first-principles calculations of the electronic structure, magnon excitations, and phonons in magnetite (Fe_3O_4), jacobsite (MnFe_2O_4), and mixed manganese–zinc ferrites ($(\text{Mn}_x, \text{Zn}_{1-x})\text{Fe}_2\text{O}_4$) for representative compositions ($0 \leq x \leq 1$) and A/B-site cation arrangements. Electronic structures are computed using density functional theory (DFT) augmented by rotationally invariant DFT+U+J, with on-site Hubbard and Hund’s parameters, U and J , respectively, determined self-consistently by spin-polarized linear-response perturbations of the chosen correlated subspaces (including, where applied, the ligand $2p$ subspace). A classical Heisenberg spin Hamiltonian is parameterized by mapping DFT+U+J total energies for multiple collinear spin configurations onto nearest-neighbor exchange couplings, which are then used to obtain magnon dispersions and magnon densities of states within linear spin-wave theory. Phonon spectra and densities of states are obtained from finite-displacement force constants and dynamical matrices computed on the same DFT+U+J-relaxed structures. Overall, the workflow provides a consistent, composition- and configuration-aware route to electronic, vibrational, and magnetic excitation spectra across the Mn/Zn ferrite space.

Keywords

spinel ferrites; DFT+U+J relaxed structures; Hubbard parameter, Hund’s exchange parameter; linear spin wave theory (LSWT); density of states

1 Introduction

Ferrites or ferrimagnetic oxides ($\text{MeO} \cdot \text{Fe}_2\text{O}_3$, $\text{Me} = \text{Mn, Fe, Co, Ni, Zn, etc.}$) underpin many high-frequency magnetic components such as inductors, transformers, and coupled electronic devices because their large resistivity, tunable ferrimagnetism, and chemical robustness mitigate conduction losses while sustaining useful permeability at higher switching frequencies and elevated operating temperatures [1, 2]. Within this class, spinel ferrites are especially attractive since they accommodate mixed-valence transition metals on crystallographically distinct tetrahedral (A sites) and octahedral (B sites) sublattices, allowing composition and cation distribution to be engineered for specific operating windows. For comparison purposes, the focus in this study is on a set of different chemistries, namely, Fe_3O_4 (magnetite), MnFe_2O_4 (Mn ferrite or jacobsite), and $(\text{Mn}_x, \text{Zn}_{1-x})\text{Fe}_2\text{O}_4$ for $x = 0.5$ (mixed Mn–Zn ferrite). These are chosen because they share the spinel motif with magnetite yet differ systematically in their cation chemistry and magnetic behavior (e.g., non-magnetic Zn^{2+} on A sites versus $\text{Mn}^{2+/3+}$ or $\text{Fe}^{2+/3+}$ on A/B sites) [3].

Fe_3O_4 serves as the archetypal ferrite, providing a well-characterized reference point for electronic structure and magnetic order. Stoichiometric Fe_3O_4 has a Curie temperature of 858 K (585 °C) and saturation magnetization (at 20 °C) of 480 kA/m [4, 5]. It is both an n-type and a p-type semiconductor. The electrical conductivity of magnetite between $10^2 - 10^3 \Omega^{-1}\text{cm}^{-1}$ is almost metallic [6, 7]. Building on this, MnFe_2O_4 in its bulk or near-bulk stoichiometric form, has a Curie temperature in the range of 570–600 K (300–400 °C), saturation magnetization

in some cases of 450–550 kA/m) [4] though nanoparticles and non-stoichiometric variants tend to reduce these values [8]. The MnFe_2O_4 is far better insulator than magnetite with its electrical conductivity between $10^{-2} - 10^{-4} \Omega^{-1}\text{cm}^{-1}$ depending on the processing route [9]. At the technological frontier, many Mn–Zn mixed ferrites show an initial relative permeability (μ_i) between 5,000 and 15,000 at frequencies between 10–100 kHz and have low core losses. However, this type of performance is highly sensitive to composition, grain size, resistivity, and fabrication method [10–12].

The energy losses in an inductor under an externally applied alternating electromagnetic field arise from transport phenomena. The time-alternating field drives the inductor material out of equilibrium and induces flows of charge, magnetization, and thermal energy. These flows dissipate energy in ways that depend upon frequency and give rise to phenomena such as ferromagnetic resonance [13] and temperature-dependent permeability [14]. Since each type of flow dissipates energy, the overall energy dissipation is coupled. To capture this, the electron, phonon, and magnon structures presented here will be utilized (in a subsequent contribution) by with the steepest-entropy-ascent quantum thermodynamic (SEAQT) formalism [15–20] to model the non-equilibrium transport that gives rise to hysteresis loss over an electromagnetic cycle. The SEAQT formalism employs an equation of motion for a system defined by a Hamiltonian operator that includes the electron, phonon, and magnon structures (i.e., so called energy eigenstructures) of the given material. The system state is represented by the density operator, and the dissipation operator of the equation of motion is derived using the steepest-entropy-ascent principle. Dissipative losses arise from entropy generation, which is manifested in the SEAQT framework by energy redistribution among the available energy eigenstates of the material. For a magnetic ferrite, the eigenstates are described by its electron, phonon, and magnon density of states (DOS), which constitute the energy eigenstructure.

The central question of the present contribution is how does the configuration of cations, i.e., which species occupy A versus B sites and in what proportions, modify the electronic, vibrational, and spin-wave energy eigenvalues and degeneracies (i.e., DOS) of a given material? Empirical proxies such as tabulated material conductivities, permeability, and structural parameters [5, 12] are often insufficiently transferable across compositions and A/B site arrangements because: (i) mixed valence and exchange interactions change with cationic distribution, alter-

ing the carrier density and magnetic coupling [21]; (ii) oxygen sub-lattice relaxations subtly change metal–oxygen bond lengths and angles, which modify $3d$ – $2p$ orbital overlap, super-exchange strength, and, thus, the hybridization pattern that shapes the DOS [22]; and (iii) alloying with Mn and Zn not only varies the number of available carriers but also changes their orbital character and the spectrum of excitations [23]. Consequently, reliable loss predictions for a given material chemistry and cation arrangement require microscopic, composition-aware spectra rather than generic property values. This motivates the use of computational quantum chemistry methods such as DFT and allied post-DFT calculations to compute the DOS of electrons, phonons, and magnons for the relevant material systems.

Concretely, mutually self-consistent DOS sets for Fe_3O_4 , MnFe_2O_4 , and mixed $(\text{Mn}_x, \text{Zn}_{1-x})\text{Fe}_2\text{O}_4$ for $x = 0.5$ are constructed and compared. “Mutually self-consistent” here indicates that for each material system: (1) the electronic structure and DOS are solved self-consistently with the same exchange-correlation family of functionals, compatible on-site electron-electron correlation strategy, k -point resolution, and convergence thresholds; (2) the magnon DOS (spin-exitations) are derived from Heisenberg exchange parameters mapped from the same electronic ground states and analyzed within a common spin-Hamiltonian framework; and (3) the phonon DOS is obtained from the corresponding electronic structures using a single, consistent force-constant workflow.

Despite its central role in modern electronic-structure modeling [24], approximate-DFT can struggle to describe the electronic structure and magnetic properties of transition-metal oxides such as iron oxides [25]. This difficulty is closely linked to the localized nature of the Fe $3d$ states and the substantial self-interaction error and delocalization-based errors of commonly used exchange-correlation functionals, including the local density approximation (LDA) and the generalized gradient approximation (GGA) [26]. More fundamentally, these errors reflect the challenge of capturing exchanges and correlations accurately using only density-based approximations and not explicitly solving the many-body Schrödinger equation.

To address this, DFT+U has over the past couple of decades become a widely adopted compromise between accuracy and computational cost by augmenting conventional functionals with an on-site correction that better represents Coulomb interactions among localized electrons [27]. More recently, several extensions and refinements of DFT+U have been developed with the goal of further correcting for static

correlation effects and delocalization errors [28, 29]. Within this broader context, the Hubbard model remains a useful conceptual framework for rationalizing the physics of correlated transition metal compounds [30], while a growing body of work has emphasized that Hund’s exchange parameter, J , can be essential for capturing phenomena such as Jahn-Teller distortions, emergent intra-atomic exchange, and Kondo-like behavior [30, 31]. These considerations motivate going beyond the simplified $U_{\text{eff}} = U - J$ treatment in DFT+ U_{eff} [32] to treating J explicitly on an equal footing with U as a separate exchange term rather than folding it into an effective parameter. The result is DFT+ $U+J$.

The challenge of DFT+ $U+J$ type functionals is that the U and J parameters must be specified before a calculation can be performed [33]. Because predicted energetics, electronic structure, and magnetic ordering can change substantially with these choices, obtaining reliable parameter values is essential. Another challenge is the limited transferability of U and J . Numerous studies have shown that these parameters are very sensitive to the local chemical environment and depend on the details of computational setup. For example, the choice of pseudopotentials and the definition of correlated subspace (i.e., site occupation projection scheme) can significantly alter the computed U values [29, 34]. As a result, U (and by extension J , which is often somewhat less environment-sensitive) cannot be treated as a universal material constant that can be tabulated, but instead must be determined on a case-by-case basis [35].

These challenges can be addressed by computing U and J from first principles. Here a linear response (LR) method [36] as opposed to a constrained random phase approximation (cRPA) method [37] is adopted. The former offers a favorable balance between accuracy and computational cost for the large number of configurations considered, while the latter is typically more expensive and, therefore, less compatible for high-throughput workflows. The LR method introduced by Cococcioni and coworkers [36] is based on the idea that self-interaction error and delocalization manifest in the curvature of the total energy with respect to the occupation of localized orbitals. In this framework U and J are obtained directly from the response of orbital and occupations to small on-site perturbations, yielding a procedure that is: (i) systematic, because it quantifies the corrective interaction implied by the underlying DFT functional, and (ii) predictive, because it relies only on DFT calculations rather than empirical fitting.

The following sections provide details of the approach used here, which consists of first computing

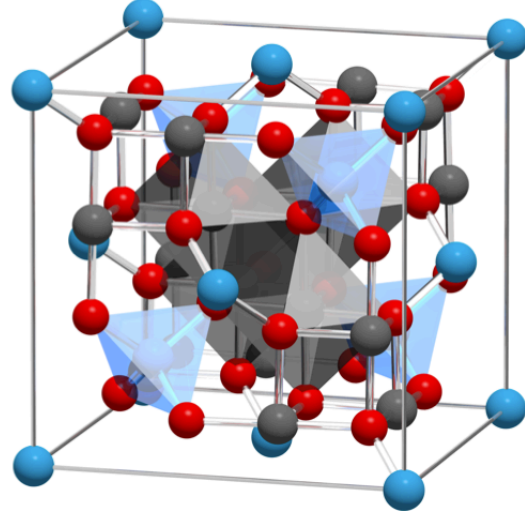


Figure 1: *Full unit cell of a spinel ferrite. Tetrahedral cations are shown in blue, octahedral cations in gray, and oxygen anions in red. The atomic radii are not shown to scale. The glass bonds show the nearest neighbor interactions.*

the U and J onsite parameters self-consistently from first principles followed by geometry optimization using the converged U and J parameters. This unified computational pipeline ensures that spectral differences reflect chemistry and cation configuration, rather than methodological artifacts. Within each composition, representative A/B cation distributions (e.g., site preferences) are examined as well to separate chemistry effects from configurational effects. The outcome is a comparative spectral map comprised of electronic, magnonic, and phononic eigenstates across Fe-, Mn-, and Mn-Zn spinel ferrites and across plausible A/B arrangements.

2 Computational Procedure

Electronic-structure, magnetic, and interatomic-force calculations are performed within DFT using the Vienna *Ab-initio* Simulation Package (**VASP**) [38–42]. Exchanges and correlations are treated using the Perdew-Burke-Ernzerhof (PBE) generalized gradient approximation [43]. Core-valence interactions are described with the projector augmented-wave (PAW) method, treating Fe $3d\,4s$ and O $2s\,2p$ as valence states. Wavefunctions are expanded in a plane-wave basis with a kinetic-energy cutoff of 500 eV. Brillouin-zone integrations use a $10 \times 10 \times 10$ Monkhorst-Pack k -point mesh [44]. Electronic self-consistency is converged to 10^{-7} eV, using Gaussian smearing

(0.005 eV). Total densities of states are evaluated with the Blöchl tetrahedron method. Structural relaxation is carried out for the conventional cubic (spinel) unit cell (space group $Fd\bar{3}m$, No. 227) containing 56 atoms (8 formula units) shown in Fig. 1. The cell shape is constrained to remain cubic, while oxygen internal coordinates are relaxed within the imposed symmetry. Cations are held at ideal crystallographic positions to preserve the target space group. Ionic relaxations employ a conjugate-gradient algorithm and are terminated when the maximum Hellmann-Feynman force falls below 10^{-6} eV Å $^{-1}$.

Spin-polarized collinear calculations are performed to represent ferrimagnetic ordering with antiparallel alignment imposed between tetrahedral (A) and octahedral (B) sub-lattices as an initial condition. Site-resolved charges and magnetic moments are obtained from a Bader partitioning of the converged densities rather than from integration within fixed atom-centered spheres. In Bader analysis, real space is divided into atomic basins bounded by zero-flux surfaces of the charge-density gradient [45]. Bader charges are computed by integrating the (PAW-reconstructed) electron density over each Bader basin, and Bader magnetic moments by integrating the spin magnetization density over the same basins (“Bader magnetization”) [46–48]. Spin-orbit interactions are not included.

2.1 The Hubbard functional for correlated electrons

The DFT+U+J approach is a corrective extension of a base (semi-)local DFT functional in which an explicit on-site interaction term is added for a chosen set of localized orbitals (the “Hubbard subspaces”) and a corresponding double-counting contribution is subtracted [26]. The resulting total-energy functional can be written as

$$\begin{aligned} E_{\text{DFT+U+J}}[\rho, \{\mathbf{n}_\iota^\sigma\}] &= E_{\text{DFT}}[\rho] + E_{\text{Hub}}[\{\mathbf{n}_\iota^\sigma\}] - E_{\text{dc}}[\{n_\iota^\sigma\}] \\ &\equiv E_{\text{DFT}}[\rho] + E_{U,J}[\{\mathbf{n}_\iota^\sigma\}], \end{aligned} \quad (1)$$

where ι indexes the Hubbard sites (typically atomic sites), $\sigma \in \{\uparrow, \downarrow\}$, and the spin-resolved on-site occupation matrices are

$$(\mathbf{n}_\iota^\sigma)_{mm'} = \langle \phi_{\iota m} | \hat{\rho}^\sigma | \phi_{\iota m'} \rangle. \quad (2)$$

Here $\{\phi_{\iota m}\}$ denotes a set of localized orbitals spanning the correlated subspace on site ι (e.g., the

transition-metal 3d manifold), and m labels the orbital quantum numbers within that subspace. The corresponding spin- and site-resolved occupations are given by

$$n_\iota^\sigma = \text{Tr } \mathbf{n}_\iota^\sigma, \quad n_\iota = n_\iota^\uparrow + n_\iota^\downarrow. \quad (3)$$

To capture anisotropic Coulomb and exchange interactions in a rotationally invariant manner, the DFT+U+J functional introduced by Liechtenstein *et al.* is used [49]. In this formulation, the Hubbard interaction energy can be expressed in terms of Coulomb matrix elements projected onto the localized-orbital basis such that

$$\begin{aligned} E_{\text{Hub}} &= \frac{1}{2} \sum_{\{m\}, \iota, \sigma} \langle m, m'' | V_{ee} | m', m''' \rangle (n_\iota^\sigma)_{mm'} (n_\iota^{-\sigma})_{m''m'''} \\ &+ \frac{1}{2} \sum_{\{m\}, \iota, \sigma} \left\{ \langle m, m'' | V_{ee} | m', m''' \rangle \right. \\ &\quad \left. - \langle m, m'' | V_{ee} | m''', m' \rangle \right\} (n_\iota^\sigma)_{mm'} (n_\iota^\sigma)_{m''m'''} \end{aligned} \quad (4)$$

where the $\langle \cdot | V_{ee} | \cdot \rangle$ are the Coulomb integrals within the correlated subspace. The double-counting term approximately removes the portion of these interactions already included in the base XC functional. In the fully localized limit (FLL) form commonly used for insulating/ionic regimes,

$$E_{\text{dc}} = \sum_\iota \frac{U_\iota}{2} n_\iota (n_\iota - 1) + \sum_{\iota, \sigma} \frac{J_\iota}{2} n_\iota^\sigma (n_\iota^\sigma - 1), \quad (5)$$

so that the corrective functional is parameterized by U_ι and J_ι [26, 49, 50].

2.2 Spin-polarized linear response

In the LR approach, on-site interaction parameters are obtained by applying small localized perturbations to the correlated subspaces and measuring the induced changes in their occupations [36]. For a set of Hubbard sites $\{\iota\}$, the site projector is defined as

$$\hat{P}_\iota = \sum_m |\phi_{\iota m}\rangle \langle \phi_{\iota m}|, \quad (6)$$

and an external on-site potential of the form

$$\hat{V} = \sum_\iota v_\iota \hat{P}_\iota. \quad (7)$$

is applied. The constrained energy associated with these perturbations can be written as

$$E[\{v_\iota\}] = \min_\rho \left\{ E[\rho] + \sum_\iota v_\iota n_\iota \right\}, \quad (8)$$

where $n_\iota = n_\iota^\uparrow + n_\iota^\downarrow$ is the total occupation of the correlated subspace on site ι . The central quantities are the (charge-channel) response matrices

$$\chi_{\iota\iota'} = \frac{\partial n_\iota}{\partial v_{\iota'}}, \quad \chi_{\iota\iota'}^{(0)} = \left. \frac{\partial n_\iota}{\partial v_{\iota'}} \right|_{\text{unscreened}}, \quad (9)$$

where χ is the fully self-consistent (screened) response and $\chi^{(0)}$ is the unscreened response, which is typically evaluated from the non-self-consistent step before Hartree+XC screening fully develops. The Hubbard parameter associated with site ι is then obtained from the difference between the inverse unscreened and screened responses such that

$$U_\iota = \left([\chi^{(0)}]^{-1} - \chi^{-1} \right)_\iota. \quad (10)$$

Note that VASP adopts an opposite sign convention for χ . The description here adopts the sign convention used by the foundational LR literature [36]. The above procedure yields the charge-channel interaction U , because the perturbation shifts the two spin channels equally ($v_\iota^\uparrow = v_\iota^\downarrow$) and the measured response is the change in total occupation n_ι .

To obtain J , a *spin-dependent* (exchange-field-like) perturbation that splits the two spin channels with opposite sign is applied so that

$$\hat{V}^\sigma = \sum_\iota v_\iota^\sigma \hat{P}_\iota, \quad v_\iota^\uparrow = +b_\iota, \quad v_\iota^\downarrow = -b_\iota. \quad (11)$$

In this case, the natural response variable is the local subspace magnetization expressed as

$$m_\iota = n_\iota^\uparrow - n_\iota^\downarrow, \quad (12)$$

and the *spin-channel* response matrices are given by

$$\chi_{\iota\iota'}^m = \frac{\partial m_\iota}{\partial b_{\iota'}}, \quad (\chi_0^m)_{\iota\iota'} = \left. \frac{\partial m_\iota}{\partial b_{\iota'}} \right|_{\text{unscreened}}. \quad (13)$$

The Hund's parameter on site ι is then obtained in direct analogy with Eq. 10 as

$$J_\iota = - \left([\chi_0^m]^{-1} - [\chi^m]^{-1} \right)_\iota, \quad (14)$$

which isolates the screened on-site exchange interaction associated with spin polarization within the correlated subspace. Note that there is an additional negative sign for the expression of J as originally proposed [29, 37, 51, 52].

2.3 Calculation of U and J

The site- and species-resolved U and J parameters are determined self-consistently for each ferrite composition and cation arrangement considered in this work using an iterative geometry-parameter feedback procedure. Starting from an initial structure (experimental lattice constant when available, otherwise a reasonable literature/relaxed starting point), a structural relaxation is first performed using the base GGA functional without Hubbard corrections. Linear-response calculations are then carried out to extract the on-site interaction parameters following the method outlined in subsection 2.2. The resulting $\{U_\iota, J_\iota\}$ values are subsequently used in a new relaxation employing the rotationally invariant DFT+U+J functional (Lichtenstein form) as implemented in VASP by setting `LDAUTYPE=3`. This cycle (relaxation \rightarrow LR extraction of $\{U, J\} \rightarrow$ updated DFT+U+J relaxation) is repeated until both the geometry and the LR-derived parameters have converged.

In the LR step, the converged ground state is perturbed by small on-site potentials applied to the localized Hubbard subspaces associated with each symmetry-inequivalent atom type present in the configuration (e.g., tetrahedral-site cations, octahedral-site cations, and oxygen). For the charge-channel response used to determine U , equal perturbations are applied to both spin channels, $v_\iota^\uparrow = v_\iota^\downarrow = \pm\alpha$, and changes in the total subspace occupancy $n_\iota = n_\iota^\uparrow + n_\iota^\downarrow$ are recorded. For the spin-channel response used to determine J , opposite-sign perturbations are applied to the two spin channels, $v_\iota^\uparrow = +\beta$ and $v_\iota^\downarrow = -\beta$, and the induced change in subspace magnetization $m_\iota = n_\iota^\uparrow - n_\iota^\downarrow$ is evaluated. For each inequivalent site/species, a set of 20 equally spaced perturbation amplitudes spanning ± 0.1 eV is used to construct the LR response matrices and extract the corresponding U_ι and J_ι [52].

2.4 The Heisenberg model

To describe magnetic excitations and extract exchange parameters from first-principles energetics, an effective Heisenberg-Dirac-van Vleck (HDvV) type spin Hamiltonian is adopted, which assumes that magnetism can be represented by a set of localized moments interacting pairwise [53, 54]. In its general bilinear form, it can be written as

$$\hat{\mathcal{H}} = - \sum_{i \neq j} \hat{\mathbf{S}}_i^\top \mathbf{J}_{ij} \hat{\mathbf{S}}_j \quad (15)$$

where $\hat{\mathbf{S}}_i$ is the spin operator at magnetic site i and

J_{ij} is the (generally anisotropic) exchange tensor of rank 2. In the present work, single-ion anisotropy and Dzyaloshinskii-Moriya interactions are not retained. The exchange tensor is, therefore, reduced to an isotropic scalar J_{ij} [55]. For collinear configurations, it is convenient to map total energies onto a classical (or, alternatively, mean-field) version of the HDvV Hamiltonian (denoted by H) by replacing spin operators with classical vectors $\mathbf{S}_i = S_i \mathbf{e}_i$ of fixed magnitude S_i and direction \mathbf{e}_i . The result is

$$H = - \sum_{i \neq j} J_{ij} \mathbf{S}_i^\top \mathbf{S}_j \quad (16)$$

This energy-mapping strategy of evaluating DFT energies for several chosen spin configurations and fitting the parameters of an effective spin Hamiltonian is widely used and is complementary to approaches based on infinitesimal spin rotations (or, magnetic force theorem) [55–57]. The present model is restricted to nearest-neighbor (NN) couplings on the spinel lattice, and the corresponding effective NN exchange constants used in subsequent spin-wave calculations are reported.

2.5 Determining the exchange coupling constants

In insulating and semiconducting spinel ferrites, the dominant magnetic interactions are typically *superexchange* couplings mediated by O 2p states along metal-oxygen-metal exchange paths rather than direct *d-d* overlap. The relative strengths and signs of these couplings are commonly rationalized using the Goodenough-Kanamori-Anderson rules, and for many spinel ferrites, the A-B coupling is the strongest and antiferromagnetic, producing ferrimagnetic order [58, 59]. Motivated by classic experimental analyses of spinel ferrites [60], the nearest-neighbor exchange network is parameterized here by three effective constants: J_{AB} for nearest-neighbor bonds between tetrahedral (A) and octahedral (B) sub-lattices, J_{AA} for nearest-neighbor A-A bonds on the diamond sub-lattice, and J_{BB} for nearest-neighbor B-B bonds on the pyrochlore sub-lattice.

Nearest-neighbor Hamiltonian on the spinel lattice: Let A and B denote the sets of A- and B-sub-lattice sites in the crystallographic cell used for the mapping. Only *magnetic* cations are included in the sums. Non-magnetic Zn is naturally handled by setting $S_i = 0$ on Zn sites (so bonds involving Zn contribute zero). For collinear reference states, the Ising variables $\sigma_i = \pm 1$ that encode whether the moment

on site i is parallel (+1) or antiparallel (-1) to a chosen global axis are introduced. The NN Heisenberg Hamiltonian for mapping is then

$$\begin{aligned} H = & -J_{AB} \sum_{\langle i \in A, j \in B \rangle} \mathbf{S}_i^\top \mathbf{S}_j \sigma_i \sigma_j \\ & - J_{AA} \sum_{\langle i, i' \in A \rangle} \mathbf{S}_i^\top \mathbf{S}_{i'} \sigma_i \sigma_{i'} \\ & - J_{BB} \sum_{\langle j, j' \in B \rangle} \mathbf{S}_j^\top \mathbf{S}_{j'} \sigma_j \sigma_{j'} \end{aligned} \quad (17)$$

where $\langle \dots \rangle$ denotes sums over nearest-neighbor bonds in the spinel lattice. With the sign convention used in Eq. 17, $J > 0$ favors ferromagnetic alignment, and $J < 0$ favors antiferromagnetic alignment.

Bond-weighted sums valid for Fe_3O_4 , Mn ferrite, and Mn-Zn ferrite: For a given chemical configuration (including the specific A/B occupation pattern), the bond-weighted NN sums are defined as

$$\begin{aligned} W_{AB} &= \sum_{\langle i \in A, j \in B \rangle} S_i S_j \\ W_{AA} &= \sum_{\langle i, i' \in A \rangle} S_i S_{i'} \\ W_{BB} &= \sum_{\langle j, j' \in B \rangle} S_j S_{j'} \end{aligned} \quad (18)$$

These quantities reduce to the familiar “bond counts times sub-lattice moments” when all magnetic sites on a sub-lattice share the same magnitude where, for example, Fe_3O_4 treated with a uniform S_A and S_B yields $W_{AB} = N_{AB} S_A S_B$, $W_{AA} = N_{AA} S_A^2$, $W_{BB} = N_{BB} S_B^2$, with $N_{AB} = 12$, $N_{AA} = 2$, $N_{BB} = 6$ per formula unit for the spinel NN topology [61].

For mixed-cation cases, Eq. 18 automatically incorporates the correct weighting. Equivalently, the A-B weight may be written as a sum over pair types. For MnFe_2O_4 , this results in

$$W_{AB} = \sum_{s \in \{\text{Fe, Mn}\}} \sum_{t \in \{\text{Fe, Mn}\}} N_{AB}^{(s_A, t_B)} S_{s_A} S_{t_B}, \quad (19)$$

and for Mn-Zn ferrites the same form applies with $t \in \{\text{Fe, Mn, Zn}\}$ but $S_{\text{Zn}} = 0$ so that Zn-containing bonds do not contribute. Analogous pair-type decompositions hold for W_{AA} and W_{BB} .

Energy mapping and closed-form expressions for J_{AB} , J_{AA} , and J_{BB} : Collinear DFT total energies are computed on the same relaxed structure for a set of reference spin states and energy *differences* are mapped onto Eq. 17 (energy-mapping analysis) [55, 57, 62]. The four reference states used are

- (i) ferrimagnetic FiM ($A\uparrow, B\downarrow$);
- (ii) ferromagnetic FM ($A\uparrow, B\uparrow$);
- (iii) an A-sublattice antiferromagnetic state A_{AF} (A Néel order on the diamond net; B is kept collinear);
- (iv) a B-sublattice antiferromagnetic state B_{AF} (collinear “2-up/2-down” arrangement on each pyrochlore tetrahedron; A is kept collinear).

For any reference state k , the bond-correlation sums are defined as

$$\begin{aligned} C_{AB}^{(k)} &= \sum_{\langle i \in A, j \in B \rangle} S_i S_j \sigma_i^{(k)} \sigma_j^{(k)}, \\ C_{AA}^{(k)} &= \sum_{\langle i, i' \in A \rangle} S_i S_{i'} \sigma_i^{(k)} \sigma_{i'}^{(k)}, \\ C_{BB}^{(k)} &= \sum_{\langle j, j' \in B \rangle} S_j S_{j'} \sigma_j^{(k)} \sigma_{j'}^{(k)} \end{aligned} \quad (20)$$

The DFT energy differences relative to FiM then satisfy

$$\begin{aligned} \Delta E_k &\equiv E_k - E_{FiM} \\ &= -J_{AB} \left(C_{AB}^{(k)} - C_{AB}^{(FiM)} \right) \\ &\quad - J_{AA} \left(C_{AA}^{(k)} - C_{AA}^{(FiM)} \right) \\ &\quad - J_{BB} \left(C_{BB}^{(k)} - C_{BB}^{(FiM)} \right) \end{aligned} \quad (21)$$

This form is completely general and remains valid for Fe_3O_4 , $MnFe_2O_4$, and $Mn-Zn$ ferrites because the chemical configuration enters only through the site magnitudes $\{S_i\}$ and the bond lists.

A particularly simple closed form exists for J_{AB} using FiM and FM because these two states have identical A-A and B-B correlations, while every A-B bond changes sign. Since $C_{AB}^{(FM)} = +W_{AB}$ and $C_{AB}^{(FiM)} = -W_{AB}$,

$$J_{AB} = -\frac{E_{FM} - E_{FiM}}{2 W_{AB}}. \quad (22)$$

The remaining constants are obtained from A_{AF} and B_{AF} . For A_{AF} the A-A nearest-neighbor bonds on the diamond net flip sign so that $C_{AA}^{(A_{AF})} = -W_{AA}$, while the A-B correlation $C_{AB}^{(A_{AF})}$ is evaluated from Eq. 20 for the imposed collinear pattern. This is important in mixed-cation cases where perfect cancellation is not guaranteed by symmetry alone. Substituting into Eq. 21 yields

$$J_{AA} = \frac{\Delta E_{A_{AF}} + J_{AB} \left(C_{AB}^{(A_{AF})} + W_{AB} \right)}{2 W_{AA}}. \quad (23)$$

Similarly, for B_{AF} the B-B correlations change and are evaluated explicitly from Eq. 20. The result is

$$J_{BB} = -\frac{\Delta E_{B_{AF}} + J_{AB} \left(C_{BB}^{(B_{AF})} + W_{BB} \right)}{C_{BB}^{(B_{AF})} - W_{BB}}. \quad (24)$$

When all B-site moments have equal magnitude and the ideal “2-up/2-down” pattern is used, such as in Fe_3O_4 , $C_{BB}^{(B_{AF})} = -(1/3)W_{BB}$, so that Eq. 24 reduces to,

$$J_{BB} = \frac{3}{4} \frac{\Delta E_{B_{AF}} + J_{AB} W_{AB}}{W_{BB}} \quad (25)$$

In $MnFe_2O_4$ and $Mn-Zn$ ferrites, the general form of Eq. 24 is retained and $C_{BB}^{(B_{AF})}$ (and any residual $C_{AB}^{(B_{AF})}$) is evaluated directly from the imposed collinear configuration.

Finally, it is emphasized that the NN three-parameter model produces *effective* exchange constants that are appropriate for the chosen lattice, composition, and cation arrangement. If further-neighbor interactions are non-negligible, the fitted NN constants should be interpreted as renormalized values within the reduced model [57].

2.6 Magnon calculations

Magnon (spin-wave) spectra are computed within linear spin-wave theory (LSWT) using the NN isotropic Heisenberg Hamiltonian on the spinel lattice described in the previous section. LSWT describes small transverse fluctuations about a long-range ordered reference state by mapping spin operators to bosons via the Holstein-Primakoff transformation and retaining only the quadratic (harmonic) terms, i.e., the leading order in a $1/S$ expansion [63, 64]. This approximation is appropriate here because the goal is to quantify how changes in cation configuration modify the *harmonic* magnon eigenvalue spectrum and its DOS.

The exchange constants $\{J_{AB}, J_{AA}, J_{BB}\}$ are taken directly from the DFT energy-mapping procedure described in the previous section and, therefore, correspond to the same relaxed crystal structure and collinear ferrimagnetic alignment (moments parallel within each sub-lattice and antiparallel between A and B). The mapping yields *effective* nearest-neighbor exchanges for each specific composition and

the A/B occupation pattern. Non-magnetic Zn is naturally accommodated in the subsequent spin-wave calculation by assigning a zero moment on Zn sites.

Spin-wave calculations are performed with **SpinW** [65]. The crystallographic lattice and magnetic basis are constructed from the DFT-optimized conventional spinel cell to ensure consistency with the structural and vibrational models. Exchange parameters are supplied in meV using the opposite sign convention and normalization adopted in the Heisenberg mapping for how these are defined within the **SpinW** code. Unless stated otherwise, Landé g factors are set to $g = 2.0$ for all magnetic cations.

In LSWT and its implementation in **SpinW**, the quadratic bosonic Hamiltonian in reciprocal space is obtained by Fourier transforming the exchange network and then diagonalized at each wavevector by a bosonic Bogoliubov transformation [65, 66]. Single-ion anisotropy and Dzyaloshinskii-Moriya interactions are neglected in the present work. This is consistent with the “soft-ferrite” character of Mn–Zn ferrites (nearly zero magnetocrystalline anisotropy) and with the general expectation that antisymmetric exchange is typically a weak correction compared with the dominant symmetric exchange in bulk materials [12, 67]. Where relevant to magnetite, spin-wave measurements provide a useful experimental context for the exchange-dominated spectra [68].

Brillouin-zone integration is performed on a uniform $15 \times 15 \times 15$ q -point mesh, and convergence is checked against $10 \times 10 \times 10$ and $12 \times 12 \times 12$ meshes. The dominant peak positions change by less than 5 meV upon refinement. The discrete spectrum is broadened with a Gaussian of width 0.05 meV to obtain a smooth mDOS. Reducing the width to 0.01 meV does not materially change the peak locations or the integrated spectral weight.

2.7 Phonon calculations

The phonon DOS for each material is computed using the finite-displacement (supercell) method as implemented in **Phonopy**, with interatomic force constants obtained from first-principles Hellmann-Feynman forces computed in **VASP** [69–71]. In this approach, small symmetry-adapted displacements are applied to crystallographically inequivalent atoms in a supercell. The resulting forces are used to assemble the real-space force-constant matrix from which the dynamical matrix is constructed and diagonalized to obtain phonon frequencies throughout the Brillouin zone [70, 71].

For each configuration, a $2 \times 2 \times 2$ supercell of the conventional spinel cell (448 atoms) is built and each

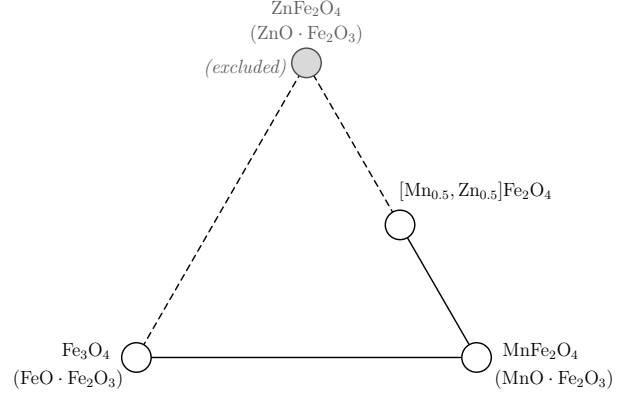


Figure 2: *Pseudo-ternary map with markers indicating studied compositions. The dashed segments indicate directions toward the excluded ZnFe_2O_4 end member.*

symmetry-inequivalent atom displaced by ± 0.01 Å along Cartesian directions. Using the same crystallographic reference and A/B occupation pattern as in the magnetic model ensures that differences in phonon spectra reflect the chemistry and cation configuration rather than changes in the underlying lattice description. Forces are evaluated for each displaced structure using the converged LR parameters (U and J) and a $3 \times 3 \times 3$ k -point mesh for the supercell. The resulting force constants are symmetrized in **Phonopy** and used to compute the phonon DOS on a $15 \times 15 \times 15$ q -mesh. No imaginary frequencies are observed for the relaxed structures, and the phonon frequencies converge to within 0.05 meV with respect to the Brillouin-zone sampling and displacement amplitude.

3 Discussion

This section organizes the outputs of the unified workflow (section 2) and frames them in a consistent way for cross-composition and cross-configuration comparison. The focus is on three spinel ferrites relevant to soft-magnetic applications: Fe_3O_4 , MnFe_2O_4 , and $(\text{Mn}_{0.5}, \text{Zn}_{0.5})\text{Fe}_2\text{O}_4$. Rather than surveying the full compositional and configurational space, the computational setup is fixed and the comparison restricted to a compact, representative set of cation arrangements so that observed trends can be traced to chemistry and local coordination rather than to methodological differences.

3.1 Structural properties

To organize the chemistry, the pseudo-ternary map in Fig. 2 is used. Its three vertices are the spinel

end members written as MeFe_2O_4 (equivalently $\text{MeO}\cdot\text{Fe}_2\text{O}_3$) formula units: Fe_3O_4 ($\text{FeO}\cdot\text{Fe}_2\text{O}_3$), MnFe_2O_4 ($\text{MnO}\cdot\text{Fe}_2\text{O}_3$), and ZnFe_2O_4 ($\text{ZnO}\cdot\text{Fe}_2\text{O}_3$). Strictly speaking, the compounds studied are spinels of the MeFe_2O_4 family, not literal mixtures of monoxides, but this triangular framing provides a useful compass for the chemistry where Fe_3O_4 sits near the Fe-rich vertex, MnFe_2O_4 steps along the $\text{Fe} \leftrightarrow \text{Mn}$ edge, and $(\text{Mn}_{0.5}, \text{Zn}_{0.5})\text{Fe}_2\text{O}_4$ marks a deliberate excursion toward the Zn corner with a fixed 1:1 Mn/Zn ratio. This triangle is used as an organizing motif rather than a thermodynamic phase diagram. It visualizes substitution paths without implying that every interior point is sampled or even synthetically accessible. Throughout, only the discrete compositions and cation configurations explicitly computed are compared, because site preference and cation inversion constrain which distributions are physically relevant. Here, “inversion” refers to the redistribution of cations between the tetrahedral (A) and octahedral (B) sub-lattices relative to the *normal* spinel arrangement and is conveniently quantified by an inversion parameter δ (fraction of the nominal A-site cations occupying B sites), with $\delta = 0$ for a normal spinel and $\delta = 1$ for a fully inverse spinel.

Within each composition, a small set of cation distributions over tetrahedral (A) and octahedral (B) sub-lattices is considered to separate chemical substitution effects from configurational effects. Fe_3O_4 serves as the canonical reference spinel, including the inequivalent B-site electronic character captured by the relaxed cubic cell. For MnFe_2O_4 , a low-inversion limit (Mn predominantly on A, $\delta \approx 0$) is compared against a more mixed distribution of Mn among A and B sites to reveal how inversion reshapes local coordination and exchange pathways. For $(\text{Mn}_{0.5}, \text{Zn}_{0.5})\text{Fe}_2\text{O}_4$, three symmetry-distinct arrangements consistent with Zn’s strong tendency toward A-site occupancy are examined [72–74], while varying how Mn is partitioned between A and B sites.

Although ZnFe_2O_4 is the natural third end member of the map in Fig. 2, it is not treated as a primary target in this work. In the normal spinel limit, Zn^{2+} occupies A sites and carries no magnetic moment, while Fe^{3+} resides on B sites. This suppresses the dominant A-B superexchange channel that underpins ferrimagnetic spinels such as Fe_3O_4 and MnFe_2O_4 [72]. As a consequence, the magnetic response of ZnFe_2O_4 is unusually sensitive to inversion and defect chemistry and is governed largely by B-B interactions [75]. Here, instead, the focus is on compositions where Zn is introduced alongside magnetic cations (Mn, Fe) so that the A-B exchange network remains active and the extracted exchange constants and magnon spec-

tra stay directly comparable across the set.

Table 1 reports the LR interaction parameters used in the DFT+U+J description, resolved by species and by A/B sub-lattice. These parameters are obtained self-consistently alongside geometry convergence. Starting from a trial parameter set, the cubic cell is relaxed under the imposed structural constraints (fixed cation framework with oxygen internal coordinates allowed to be adjusted). The LR is then performed on that relaxed state to update (U, J) for each inequivalent subspace, and the relaxation is repeated using the updated values. This relaxation-LR cycle is continued until both the structural descriptors (e.g., a , u for geometry) and the LR parameters change negligibly between successive iterations. With that closed loop and identical numerical settings for every case, trends in Table 1 can be interpreted as environmental screening trends tied to local coordination, rather than as artifacts of inconsistent parametrization.

The inclusion of oxygen in the LR analysis is intentional. In spinel ferrites, the electronic structure and magnetic superexchange are controlled by $\text{Fe}/\text{Mn}(3d) - \text{O}(2p)$ hybridization. Oxygen is, therefore, the dominant screening and mediation channel for the correlated d subspaces and exchange pathways. Performing LR on the O(2p) subspace provides a consistent way to quantify how the ligand network participates in screening within the same projector definition used for the cations [29, 35, 51]. In Table 1, U_{Oxygen} is comparatively large (near 10 eV across all compositions) and varies only weakly from one configuration to another. In the present context, this should be read less as a ‘standalone oxygen correlation strength’ and more as a stability indicator of the ligand screening environment under a fixed LR definition, namely, that the ligand framework remains broadly comparable across the series, while most configuration sensitivity enters via which cations occupy A and B sites and how that redistributes $d-p$ hybridization locally [76, 77].

A key point for interpreting Table 1 is that the LR-extracted J is an effective on-site exchange parameter within the chosen Hubbard functional and projector subspace, not a direct measurement of the bare atomic Hund’s coupling. Within LR, U and J are obtained by fitting the curvature of the total energy with respect to controlled perturbations of on-site occupations (and, depending on the implementation, spin-resolved occupations). In strongly covalent or highly screened environments, particularly for $\text{Fe}-d$ subspaces hybridized with O- p , this effective J can become negative without implying a literal reversal of Hund’s rule on the atom. Rather, a negative value

Table 1: Linear-response results: on-site Hubbard U and Hund’s exchange J parameters for each inequivalent site. “50/50 Mn on A & B” means half of the Mn on A sites and half of the Mn on B sites.

(a) Fe_3O_4

Configuration	Fe-A	Fe-B	O
Prototype	$U = 4.491$ $J = -0.488$	$U = 5.235$ $J = -1.316$	$U = 10.146$ $J = 1.209$

(b) MnFe_2O_4

Configuration	Mn-A	Mn-B	Fe-A	Fe-B	O
Config. 1 (all Mn on A)	$U = 5.968$ $J = 0.203$	N/A	N/A	$U = 4.974$ $J = -0.547$	$U = 9.881$ $J = 1.072$
Config. 2 (50/50 Mn on A & B)	$U = 5.637$ $J = 0.335$	$U = 5.640$ $J = 0.529$	$U = 5.617$ $J = -2.740$	$U = 5.069$ $J = -1.060$	$U = 10.083$ $J = 1.152$

(c) $(\text{Mn}_{0.5}, \text{Zn}_{0.5})\text{Fe}_2\text{O}_4$

Configuration	Zn-A	Mn-A	Mn-B	Fe-A	Fe-B	O
Config. 1 (all Zn & Mn on A)	$U = 2.017$ $J = 0.013$	$U = 4.075$ $J = 1.344$	N/A	N/A	$U = 5.171$ $J = -1.824$	$U = 10.126$ $J = 1.181$
Config. 2 (all Zn on A, all Mn on B))	$U = 2.645$ $J = 0.287$	N/A	$U = 5.701$ $J = 0.466$	$U = 4.866$ $J = -0.849$	$U = 4.982$ $J = -0.042$	$U = 10.037$ $J = 1.121$
Config. 3 (all Zn on A, 50/50 Mn on A & B)	$U = 3.670$ $J = 0.981$	$U = 5.788$ $J = 0.318$	$U = 6.701$ $J = 0.188$	$U = 4.708$ $J = -0.443$	$U = 5.029$ $J = -0.758$	$U = 10.068$ $J = 1.383$

indicates that, in the effective subspace used by the functional, the exchange-like contribution that would normally be represented by a positive J is already accounted for (or over-screened) by the underlying DFT description and screening so that the LR-consistent corrective term would enter with the opposite sign to reproduce the response curvature. Practically, readers should interpret U and J as a paired parameterization of the on-site correction. In that sense, a negative J tends to increase the net on-site penalty relative to using U alone within the same functional form. In the remainder of this section, attributing atomic ‘Hund’s rule’ meaning to the sign of J is, therefore, avoided, and instead how the self-consistent parameter set varies with A/B coordination and Mn/Zn substitution is tracked as is how those changes correlate with the DOS and exchange constants.

The structural descriptors in Table 2 summarize both the global geometry and the local coordination landscape of each relaxed 56-atom cubic cell. In these relaxations, the cation framework is held fixed at the chosen A/B occupations, while the oxygen sub-lattice is allowed to relax within the imposed sym-

metry so that the lattice parameter a and oxygen internal parameter u self-consistently accommodate the cation chemistry and site distribution. Because the relaxed oxygen positions generate a set of Me–O bonds that are generally not all symmetry-equivalent (especially in chemically mixed or partially inverted configurations), each Me–O distance is reported in a statistical form, namely, the mean \pm standard deviation taken over all corresponding Me–O bonds of that species and sub-lattice within the cell. In this representation, the mean captures the typical bond scale relevant to orbital overlap and polyhedral geometry, while the spread quantifies the degree of tetrahedral/octahedral distortion induced by the fixed cation arrangement and the oxygen relaxation. These structural metrics are converged together with the LR parameters through the same relaxation-LR cycle described above so the reported bond-length statistics and the final (U, J) values are mutually consistent descriptors of the same relaxed state.

Several trends emerge directly from Table 2. Substituting Mn into the spinel expands the lattice relative to Fe_3O_4 : a increases from 8.391 Å in Fe_3O_4 to

Table 2: Structural and local descriptors for the relaxed spinel cells studied in this work. For each configuration, the lattice parameter a and oxygen internal parameter u are reported, while the bond lengths d of Me-O bond (with Me = Fe, Mn, Zn), magnetic moments μ , and Bader charges $|e|$ are listed in a site/species-resolved form.

Compound	a (Å)	u	d (Å)	μ (μ_B)	$ e $
Fe₃O₄					
Prototype	8.391	0.2567	Fe _A –O: 1.8347 ± 0.035 Fe _B –O: 2.0653 ± 0.055	Fe _A : 4.225 (\uparrow) Fe _B : 3.812/4.101 (\downarrow)	Fe _A : 2.344 Fe _B : 1.991/2.075 O: -1.623
MnFe₂O₄					
Config. 1 (all Mn on A)	8.513	0.2629	Mn _A –O: $1.9051 \pm 1.7e-5$ Fe _B –O: $2.0680 \pm 1.2e-5$	Mn _A : 4.650 (\uparrow) Fe _B : 4.322 (\downarrow)	Mn _A : 1.581 Fe _B : 1.994 O: -1.429
Config. 2 (50/50 Mn on A & B)	8.520	0.2615	Mn _A –O: 2.0463 ± 0.016 Fe _A –O: 1.9232 ± 0.065 Mn _B –O: 2.0687 ± 0.096 Fe _B –O: 2.0439 ± 0.058	Mn _A : 4.641 (\uparrow) Fe _A : 4.554 (\uparrow) Mn _B : 4.948 (\downarrow) Fe _B : 4.378/3.815 (\downarrow)	Mn _A : 1.646 Fe _A : 1.907 Mn _B : 1.487 Fe _B : 1.932/1.688 O: -1.401
(Mn_{0.5}, Zn_{0.5})Fe₂O₄					
Config. 1 (all Zn & Mn on A)	8.411	0.2582	Zn _A –O: 1.9890 ± 0.023 Mn _A –O: 1.7893 ± 0.001 Fe _B –O: 2.0670 ± 0.066	Mn _A : 4.585 (\uparrow) Fe _B : 4.774 (\downarrow)	Zn _A : 1.202 Mn _A : 1.593 Fe _B : 1.976 O: -1.397
Config. 2 (all Zn on A, all Mn on B)	8.448	0.2587	Zn _A –O: 1.9821 ± 0.019 Fe _A –O: 1.8981 ± 0.042 Mn _B –O: 2.0352 ± 0.086 Fe _B –O: 2.0561 ± 0.051	Fe _A : 4.265 (\uparrow) Mn _B : 4.644 (\downarrow) Fe _B : 4.298/3.758 (\downarrow)	Zn _A : 1.213 Fe _A : 1.839 Mn _B : 1.522 Fe _B : 1.884/1.624 O: -1.456
Config. 3 (all Zn on A, 50/50 Mn on A & B)	8.414	0.2612	Zn _A –O: 1.9818 ± 0.017 Mn _A –O: 2.0318 ± 0.018 Fe _A –O: 1.9467 ± 0.052 Mn _B –O: 2.0421 ± 0.077 Fe _B –O: 2.0299 ± 0.037	Mn _A : 4.629 (\uparrow) Fe _A : 4.237 (\uparrow) Mn _B : 4.651 (\downarrow) Fe _B : 4.353 (\downarrow)	Zn _A : 1.211 Mn _A : 1.626 Fe _A : 1.852 Mn _B : 1.591 Fe _B : 1.891 O: -1.422

8.51–8.52 Å in MnFe_2O_4 , accompanied by an increase in u (0.2567 → 0.261–0.263), indicating a modified oxygen framework and, hence, an altered Me–O–Me geometry, consistent with a more expanded cation–oxygen skeleton. The ordered MnFe_2O_4 configuration with Mn exclusively on A sites yields essentially single-valued $\text{Mn}_A\text{–O}$ and $\text{Fe}_B\text{–O}$ distances (spreads $\sim 10^{-5}$ Å), which is a direct consequence of the constrained relaxation. With a uniform cation environment and symmetry-preserving oxygen relaxation, the oxygen sub-lattice converges to nearly equivalent coordination polyhedra. By contrast, for the mixed A/B configuration, the Me–O distributions broaden substantially ($\text{Mn}_A\text{–O}$: 2.0687 ± 0.096 Å; and $\text{Fe}_B\text{–O}$: 1.9232 ± 0.065 Å), reflecting oxygen-sub-lattice distortions induced by chemical heterogeneity within the same coordination network. Across the Mn–Zn ferrite configurations, a and u shift modestly relative to Fe_3O_4 , but the bond-length spreads again consistent with how Mn is partitioned between A and B sites, signaling how the oxygen network accommodates competing site preferences.

Bader charges are reported as well as a post-processing descriptor of charge redistribution. In Bader analysis, the total electron density is partitioned into atomic basins bounded by zero-flux surfaces in $\nabla\rho(\mathbf{r})$, and the integrated charge in each basin yields an ‘atomic’ charge associated with that site. While Bader charges are not formal oxidation states and depend on the chosen density and partitioning scheme, they provide a consistent, geometry-sensitive proxy for how charge transfer and covalency trends evolve across compositions and configurations when the same workflow is used throughout [45]. In the present study they are particularly useful because the dominant physics (screening, d – p hybridization, and superexchange) depends on how electron density is shared between cations and oxygen. Bader charges, therefore, complement the LR parameters by providing an independent, density-based view of how substitution and A/B occupancy shift the electronic environment.

In Fe_3O_4 , oxygen carries the most negative Bader charge in the series (O: -1.623), while the cations span a broader range ($\text{Fe}(A)$: 2.344; $\text{Fe}(B)$: 1.99 to 2.08), consistent with non-equivalent Fe environments on the A and B sub-lattices. Upon Mn and/or Zn substitution, oxygen becomes systematically less negative (typically ~ -1.40 to -1.46), indicating a redistribution of charge density consistent with altered covalency and screening in the Me–O network under the same partitioning scheme. Zn carries the smallest positive Bader charge (~ 1.20), consistent with its closed-shell character in the present bond-

ing environment, while Mn sits near ~ 1.5 to 1.65. The Fe charges shift with site and configuration (e.g., $\text{Fe}(A) \sim 1.84$ to 1.91 in the Mn–Zn cases), reinforcing that A/B occupancy changes not only geometry but also the local electronic environment in a way that is consistent with the environment-dependent LR parameters reported in Table 1. The magnetic moments remain in the high-spin range expected for Mn and Fe in these coordinations. Taken together, the bond-length statistics and Bader charges show that ‘inversion’ is not merely a bookkeeping label, it induces measurable oxygen-sub-lattice distortions and charge redistribution that ultimately reshape exchange pathways.

Table 3 translates the relaxed local environments into nearest-neighbor Heisenberg couplings. To avoid ambiguities from differing normalizations, all exchange constants reported are extracted by the same collinear energy-mapping procedure applied to the same 56-atom cubic cell for every case, and the sign convention and units (meV) are kept identical throughout. Details of the mapping equations and alternative normalizations are deferred to subsection 2.5. Across every composition and configuration, the dominant interaction is the A–B channel, and it is consistently antiferromagnetic: J_{AB} remains negative and of largest magnitude (e.g., -2.38 meV in Fe_3O_4 , -1.88 meV in the low-inversion MnFe_2O_4 configuration, and ~ -1.38 to -2.04 meV across the Mn–Zn configurations). This uniform sign and scale establishes the ferrimagnetic backbone of the series and provides a direct structural-magnetic link, namely, changes in which species occupy A and B sites primarily modulate the strength of the A–B exchange channel rather than its character. The same-sub-lattice interactions are smaller but not negligible and show stronger chemistry dependence. The B–B couplings are uniformly ferromagnetic in this dataset and can become comparable to $|J_{AB}|$ in several mixed cases (e.g., $J_{BB} = 2.03$ meV for $\text{Fe}(B)\text{–Fe}(B)$ in mixed MnFe_2O_4 , and 2.04 meV in $(\text{Mn}_{0.5}, \text{Zn}_{0.5})\text{Fe}_2\text{O}_4$ Config. 1), indicating that the B sub-lattice network stiffens substantially in some chemically/structurally distinct octahedral environments. In contrast, the A–A interactions are generally small in magnitude in mixed configurations (typically near zero with mixed signs), but become strongly configuration-dependent when A is occupied by a single magnetic species, as seen in the ferromagnetic $\text{Mn}(A)\text{–Mn}(A)$ coupling ($J_{AA} = 0.74$ meV) in the low-inversion MnFe_2O_4 configuration. Where multiple species-resolved nearest-neighbor channels exist within the same exchange class, the table should be read channel-by-channel. The intra-class differences are precisely the finger-

Table 3: Nearest-neighbor (NN) Heisenberg exchange constants for the relaxed spinel cells studied in this work. All J_{ij} values are extracted by the same collinear energy-mapping protocol on the same 56-atom cubic cell for every compound and configuration. The convention of Eq. 16 is used. Thus, $J > 0$ favors ferromagnetic alignment and $J < 0$ favors antiferromagnetic alignment. Where multiple species-resolved NN channels exist within the same exchange class, they are listed as multiple entries within the cell.

Compound	J_{AB} (meV)	J_{BB} (meV)	J_{AA} (meV)
Fe₃O₄			
Prototype	Fe _A –Fe _B : -2.38	Fe _B –Fe _B : 0.56	Fe _A –Fe _A : -0.26
MnFe₂O₄			
Config. 1 (all Mn on A)	Mn _A –Fe _B : -1.88	Fe _B –Fe _B : 1.18	Mn _A –Mn _A : 0.74
Config. 2 (50/50 Mn on A & B)	Mn _A –Fe _B : -2.068 Fe _A –Mn _B : -1.541 Fe _A –Fe _B : -1.126 Mn _A –Mn _B : -1.730	Mn _B –Fe _B : 0.93 Mn _B –Mn _B : 1.18 Fe _B –Fe _B : 2.03	Mn _A –Fe _A : -0.020 Mn _A –Mn _A : -0.061 Fe _A –Fe _A : 0.105
(Mn_{0.5}, Zn_{0.5})Fe₂O₄			
Config. 1 (all Zn & Mn on A)	Mn _A –Fe _B : -1.94	Fe _B –Fe _B : 2.04	Mn _A –Mn _A : -0.004
Config. 2 (all Zn on A, all Mn on B)	Fe _A –Mn _B : -1.656 Fe _A –Fe _B : -1.382	Mn _B –Fe _B : 1.30 Mn _B –Mn _B : 0.83 Fe _B –Fe _B : 0.92	Fe _A –Fe _A : -0.07
Config. 3 (all Zn on A, 50/50 Mn on A & B)	Mn _A –Fe _B : -2.036 Mn _A –Mn _B : -1.247 Fe _A –Fe _B : -1.109 Fe _A –Mn _B : -1.444	Mn _B –Fe _B : 0.79 Mn _B –Mn _B : 1.37 Fe _B –Fe _B : 1.96	Mn _A –Mn _A : -0.024 Mn _A –Fe _A : 0.018 Fe _A –Fe _A : -0.008

print of local chemical heterogeneity in the fixed 56-atom cell.

With the geometric descriptors and nearest-neighbor exchange constants established on a consistent footing, the resulting electronic, vibrational, and magnon spectra across the same set of relaxed 56-atom cubic cells are compared next.

3.2 Electron density of states

In Fig. 3(a), the spin-resolved total eDOS of Fe_3O_4 is strongly asymmetric at the Fermi level since the minority channel (blue) retains finite spectral weight at fermi energy E_F , whereas the majority channel (red) is strongly suppressed, approaching a deep pseudogap. This spin-selective metallicity is consistent with the commonly reported half-metal-like electronic structure of cubic magnetite in DFT+U-type treatments (minority conducting, majority insulating/suppressed). Across all panels, the deep feature near ~ -20 eV is characteristic of the oxygen $2s$ manifold, while the broad valence complex is between roughly -9 and -2 eV while the near- E_F states are typically associated with hybridized O- $2p$ / transition-metal $3d$ weight.

In contrast, Fig. 3(b) (MnFe_2O_4 , Mn confined to A sites) shows a strong depletion of the eDOS at E_F in both spin channels, consistent with an insulating or small-gap ferrimagnetic state in this configuration. Relative to Fig. 3(a), the states that cross (or approach) the Fermi level are removed, indicating that the spin-selective metallicity of magnetite is not preserved when Mn is forced entirely onto the tetrahedral sub-lattice. Interpreting the microscopic origin (e.g., high-spin Mn^{2+} and reduced mixed-valence conduction pathways on the octahedral network) should be supported explicitly by the site-resolved moments/charges, since the total eDOS alone cannot uniquely assign oxidation states or sub-lattice-resolved itinerancy. Allowing Mn to occupy both sub-lattices (Fig. 3(c), 50/50 Mn on A and B sites) modifies the near- E_F spectrum relative to the all-A case, but the Fermi level still lies in a strongly depleted region of the total eDOS. Compared with Fig. 3(b), there is some redistribution of the spectral weight in the ~ -2 to 0 eV window, most evident in the minority channel, yet Fig. 3(c) does not recover the clear minority-metallic crossing observed for Fe_3O_4 in Fig. 3(a). On the basis of the total eDOS alone, this configuration is therefore best described as insulating/small-gap or pseudogapped, with inversion acting to reshape (and potentially narrow) the depletion around E_F rather than unambiguously

restoring a half-metallic state.

The mixed Mn-Zn ferrite cases in Fig. 3(d-f) all show a pronounced suppression of the eDOS at the Fermi level compared with magnetite, indicating that the spin-selective metallicity of Fe_3O_4 is not retained upon partial substitution by Mn/Zn and the associated cation rearrangements. In Fig. 3(d) (Mn and Zn placed on A sites), both spin channels remain strongly depleted near E_F with the spectral weight concentrated well below the Fermi level and in unoccupied features above $\sim 1 - 3$ eV. The persistence of a near- E_F depletion in both spins is consistent with an insulating/small-gap electronic structure for this cation arrangement. Placing Zn on A sites while transferring Mn to the B sub-lattice (Fig. 3(e)) does not generate an obvious metallic crossing at E_F . Instead, the Fermi level again lies within a deep depletion region for both spins. Compared with Fig. 3(d), the minority eDOS shows a stronger redistribution of states in the ~ -2 to 0 eV window, but the spectrum at E_F remains suppressed. The large unoccupied majority-spin feature above E_F (around a few eV) becomes more prominent in this configuration, indicating that the substitution/redistribution primarily reshapes the conduction-side eDOS rather than introducing robust Fermi-level carriers. The intermediate Mn partitioning case (Fig. 3(f), Zn fixed on A with Mn shared between A and B) likewise retains a depleted E_F region with only modest changes in the immediate vicinity of the Fermi level relative to Fig. 3(d-e). Taken together, Fig. 3(d-f) suggest that, within the present DFT(+U+J) description, the Mn-Zn substituted ferrites remain insulating/small-gap or pseudogapped across the tested cation distributions and that cation arrangement primarily tunes the detailed spectral weight on the valence- and conduction-side of the depletion rather than producing a magnetite-like half-metallic eDOS.

3.3 Magnon density of states

Fig. 4 presents the mDOS for the same six compositions/configurations considered in the electronic analysis. Across all cases, the mDOS turns on beginning from zero energy, consistent with a gapless acoustic branch in the absence of explicit anisotropy terms. The differences between panels are therefore dominated not by the presence or absence of a magnon gap, but by how the spectral weight is distributed over the energy and by the maximum excitation energy (the band top), both of which reflect how the exchange network and sub-lattice occupancy shape the collective spin-wave spectrum.

For Fe_3O_4 , the mDOS in Fig. 4(a) is character-

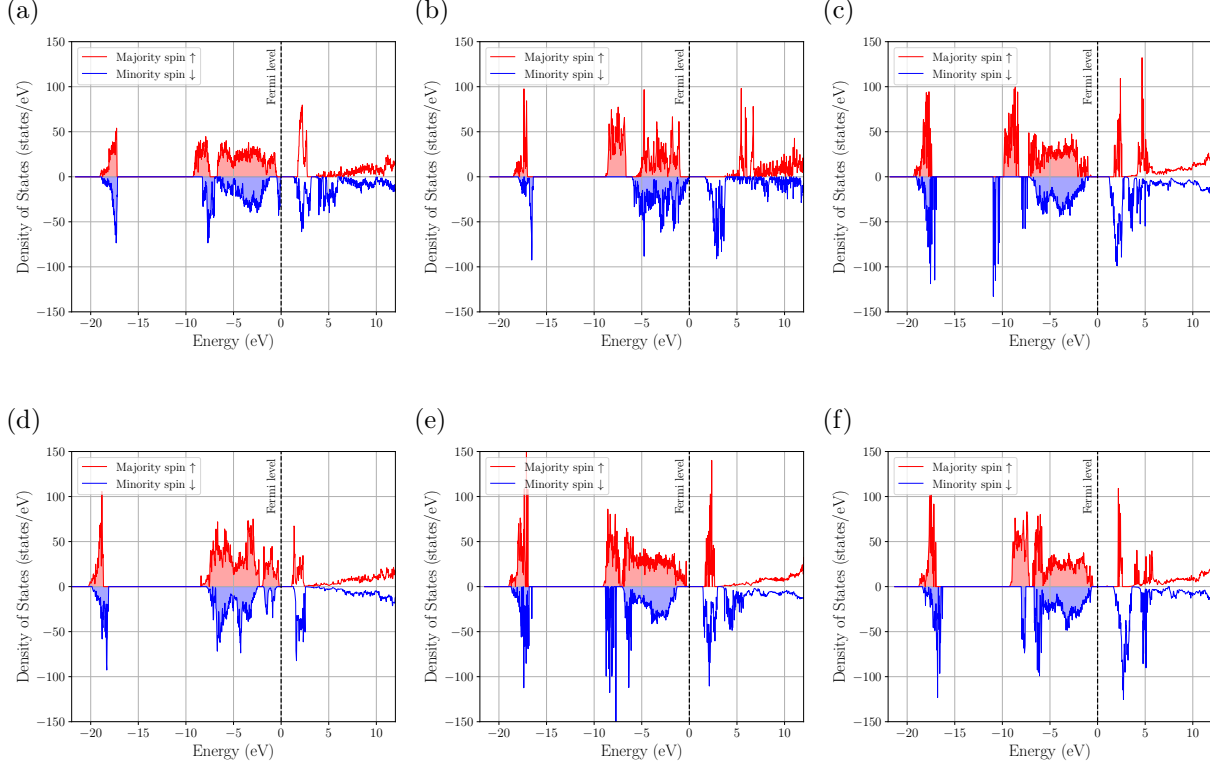


Figure 3: Electron DOS for spinel ferrites with different cationic composition and configuration. (a) archetypal Fe_3O_4 , (b) MnFe_2O_4 Config. 1 where all Mn atoms occupy A-sites of the spinel structure, (c) MnFe_2O_4 Config. 2 where half of the Mn atoms occupy A-sites and the other half occupy B-sites, (d) $(\text{Mn}_{0.5}, \text{Zn}_{0.5})\text{Fe}_2\text{O}_4$ Config. 1 where all Zn & Mn atoms occupy A-sites, (e) $(\text{Mn}_{0.5}, \text{Zn}_{0.5})\text{Fe}_2\text{O}_4$ Config. 2 where all Zn atoms occupy A-sites & all Mn atoms occupy B-sites, (f) $(\text{Mn}_{0.5}, \text{Zn}_{0.5})\text{Fe}_2\text{O}_4$ Config. 3 where all Zn atoms occupy A-sites & the Mn atoms occupy half A-sites and half B-sites.

ized by two pronounced accumulations of states separated by a substantial depletion region. The spectrum rises gradually from low energies and develops a strong, narrow peak near ~ 55 meV, followed by a region of very low mDOS through much of the upper mid-energy range. A second sharp peak appears near ~ 80 meV before the mDOS rapidly decays to near zero by $\sim 85 - 90$ meV, defining the largest bandwidth among the six panels. The appearance of two dominant ‘piles’ of modes, rather than one broad continuous hump, indicates that distinct branch families contribute strongly at separated energies, which is expected in ferrimagnets with multiple magnetic sub-lattices and multiple dispersive branches. In practical terms, Fe_3O_4 exhibits the stiffest spectrum here, with high band top and strong van-Hove-like singularities[78].

When Mn is constrained to occupy only A sites in MnFe_2O_4 , the overall bandwidth (in Fig. 4(b)) remains comparable to Fe_3O_4 shown in Fig. 4(a), but the location and continuity of the dominant spectral features change. The mDOS remains nonzero from

low energy and fills the mid-energy window more continuously than in Fe_3O_4 , culminating in a very strong singular peak near ~ 65 meV. In contrast to magnetite, the post-peak region does not exhibit an extended interval of near-zero mDOS. Rather, finite weight persists through much of the $\sim 40 - 80$ meV range, and the high-energy tail extends toward $\sim 85 - 90$ meV. Thus, the all-A Mn arrangement reorganizes the spectrum so that the dominant accumulation of modes shifts upward (from ~ 55 to ~ 65 meV) and the mDOS becomes less clearly partitioned into separated lobes.

Allowing Mn to occupy the B sub-lattice in MnFe_2O_4 produces a clear softening and compression of the magnon spectrum (Fig. 4(c)). The most prominent mDOS peak shifts downward to $\sim 42 - 45$ meV, and the upper-energy extent contracts with the mDOS approaching zero by roughly $\sim 78 - 80$ meV. Above the dominant low-energy singularity, the spectrum consists of a broad, structured band with multiple smaller peaks extending through the $\sim 50 - 75$ meV region rather than a single dominant

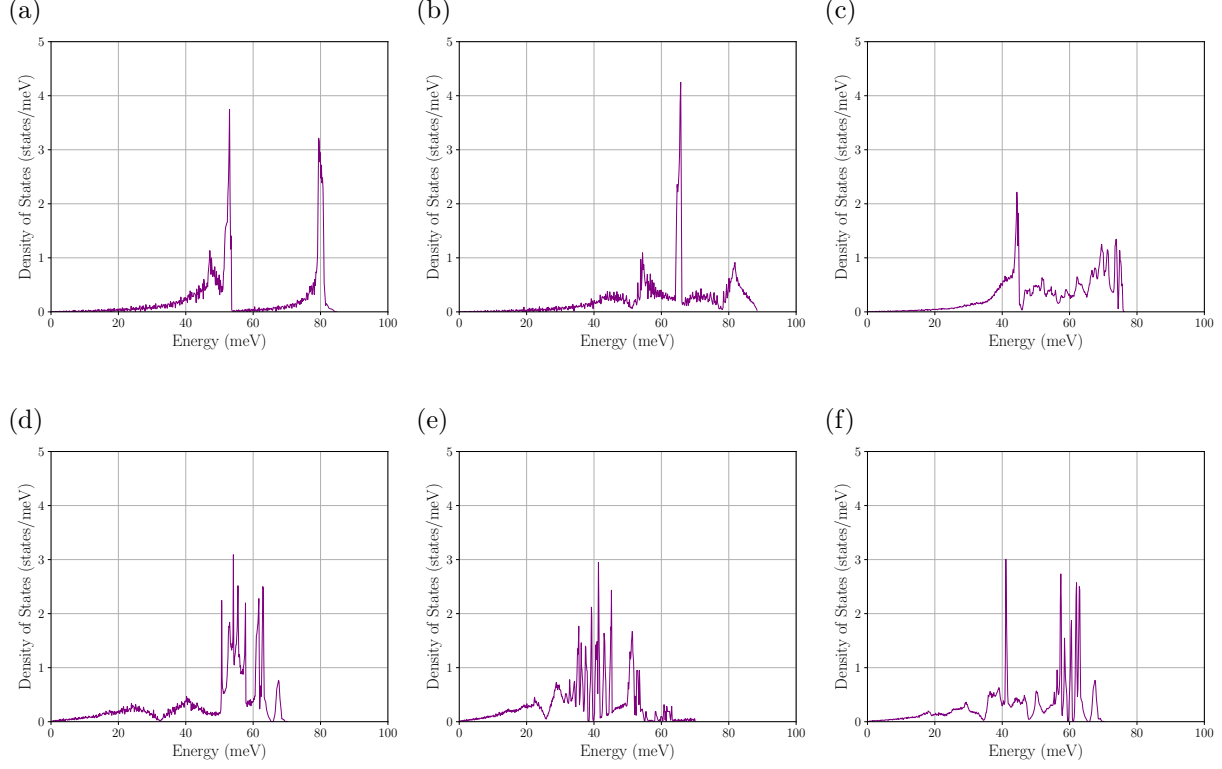


Figure 4: *Magnon DOS for spinel ferrites with different cationic composition and configuration.* (a) archetypal Fe_3O_4 , (b) $\text{Mn}\text{Fe}_2\text{O}_4$ Config. 1 where all Mn atoms occupy A-sites of the spinel structure, (c) $\text{Mn}\text{Fe}_2\text{O}_4$ Config. 2 where half of the Mn atoms occupy A-sites and the other half occupy B-sites, (d) $(\text{Mn}_{0.5}, \text{Zn}_{0.5})\text{Fe}_2\text{O}_4$ Config. 1 where all Zn & all Mn atoms occupy A-sites, (e) $(\text{Mn}_{0.5}, \text{Zn}_{0.5})\text{Fe}_2\text{O}_4$ Config. 2 where all Zn atoms occupy A-sites & all Mn atoms occupy B-sites, (f) $(\text{Mn}_{0.5}, \text{Zn}_{0.5})\text{Fe}_2\text{O}_4$ Config. 3 where all Zn atoms occupy A-sites & the Mn atoms occupy half A-sites and half B-sites.

high-energy accumulation. Relative to both Fe_3O_4 and the all-A Mn case, Fig. 4(c) shows a redistribution of spectral weight toward lower energies and a reduced band top, indicating a softer spin-wave spectrum that would be expected when the dominant exchange pathways and sub-lattice-resolved couplings are altered by inversion.

The Mn–Zn ferrite configurations further reduce the accessible magnon energy range and introduce a visibly more fragmented mDOS with many narrow spikes (Fig. 4(d)–(f)). When Mn and Zn are both placed on A sites, the spectrum in Fig. 4(d) retains a gradual low-energy rise but concentrates much of its weight into a dense cluster of sharp peaks between ~ 55 and 66 meV with the mDOS essentially vanishing by ~ 70 meV. This combination of a reduced maximum energy and a highly spiky mid-energy band indicates a compressed spectrum with strong van-Hove-like features [78, 79] consistent with the reduced magnetic connectivity expected when a nonmagnetic species (Zn) is present on one of the sub-lattices. Placing Zn on A sites while transfer-

ring Mn to B sites yields the softest-looking Mn–Zn spectrum among the three mixed cases. It is shown in Fig. 4(e). Here the mDOS already displays substantial structure and elevated weight in the ~ 20 – 45 meV window, including numerous narrow spikes, while the high-energy tail is curtailed and the mDOS dies out by roughly ~ 60 – 65 meV. Compared with the all-(Mn,Zn)-on-A configuration (Fig. 4(d)), this case shifts the spectral weight markedly downward and further compresses the bandwidth, pointing to reduced characteristic magnon energies and a higher density of low-energy excitations.

In the intermediate Mn partitioning case (Zn fixed on A with Mn distributed between A and B), the mDOS in Fig. 4(f) exhibits signatures of both preceding Mn–Zn arrangements. A sharp singular feature near ~ 40 – 42 meV reappears, while an additional cluster of spikes emerges around ~ 58 – 63 meV, and the spectrum again terminates near ~ 70 meV. This panel, therefore, shows two separated families of mode accumulations within a reduced overall bandwidth, consistent with multiple magnetic envi-

ronments arising from distributing Mn across both sub-lattices while Zn remains fixed. Taken together, the Mn–Zn results indicate that cation arrangement primarily controls the degree of softening (bandwidth reduction) and the redistribution of mDOS toward lower energies, with the Zn-containing configurations generally exhibiting lower band tops and more strongly structured (spiky) mid-energy spectra than Fe_3O_4 and MnFe_2O_4 .

3.4 Phonon density of states

In Fig. 5(a-f), the total pDOS spans approximately 0-90 meV and turns on smoothly from zero energy, consistent with acoustic modes at long wavelength. Rather than splitting into sharply isolated blocks, each spectrum exhibits multiple broad manifolds with a configuration-dependent peak structure, and all six panels share a prominent depletion (a ‘mini-gap’) centered around roughly 62-65 meV. Above this depletion, a high-energy tail extends to the band top near 90 meV with several relatively sharp features. While species-resolved assignments require projected pDOS, the higher-energy portion of the spectrum is typically associated with the oxygen-dominated stretching character, whereas the lower- and mid-energy regions contain mixed cation-oxygen bending and cation-participating modes.

For MnFe_2O_4 with Mn confined to A sites, the pDOS, shown in Fig. 5(b), rises gradually from 0 meV and develops a sequence of structured peaks throughout the low- and mid-energy range. The dominant spectral weight is concentrated between roughly 35 and 60 meV, with a particularly strong peak near ~ 50 meV and an additional pronounced structure approaching $\sim 58 - 60$ meV. A deep depletion follows at $\sim 62 - 65$ meV after which only a comparatively weaker high-energy tail persists up to the band top near ~ 90 meV. Relative to Fe_3O_4 , this configuration shifts and concentrates the mid-frequency weight (especially around 45-60 meV), while retaining the same overall bandwidth, indicating that cation arrangement reshapes the distribution of vibrational states more than it changes the maximum phonon energy. When Mn is distributed between A and B sites (see Fig. 5(c)), the phonon DOS becomes more sharply structured with a very prominent peak near ~ 40 meV that exceeds the corresponding mid-band amplitudes in Fe_3O_4 and the all-A Mn configuration. The lower-energy region also exhibits a strong group of features around $\sim 20 - 25$ meV. As in the other panels, the pDOS drops into a deep depletion near $\sim 62 - 65$ meV and then continues as a weaker high-energy tail toward ~ 90 meV. Compared with the

all-A Mn case, this configuration shifts substantial vibrational weight downward (from the 50-60 meV region toward ~ 40 meV) while preserving the overall bandwidth.

For $(\text{Mn}_{0.5}, \text{Zn}_{0.5})\text{Fe}_2\text{O}_4$ with Mn and Zn placed on A sites, the pDOS shown in Fig. 5(d) remains continuous from 0 to ~ 90 meV but shows a particularly strong mid-frequency maximum centered near $\sim 38 - 40$ meV accompanied by additional structure throughout the 45-60 meV region. The same pronounced depletion near $\sim 62 - 65$ meV is retained after which only modest high-energy features persist. Relative to the Mn-free magnetite panel, the mixed Mn–Zn configuration concentrates more spectral weight into a narrower mid-band peak near ~ 40 meV consistent with a cation-configuration-driven reshaping of intermediate-frequency vibrations. Placing Zn on A sites while forcing Mn onto B sites (see Fig. 5(e)) produces one of the strongest enhancements of low-energy weight among the Mn–Zn cases, namely, a pronounced peak already emerges near $\sim 18 - 20$ meV in addition to a broad and intense mid-band centered around $\sim 40 - 45$ meV. The deep depletion near $\sim 62 - 65$ meV again appears clearly, and the high-energy tail above it is comparatively weaker and more fragmented. This spectrum, therefore, shifts a notable fraction of vibrational density toward lower energies compared with the all-A (Mn,Zn) arrangement, indicating that which species occupies the octahedral network materially affects the placement and intensity of mid-frequency manifolds.

In the intermediate Mn partitioning case (Fig. 5(f)), the pDOS exhibits both a strong low- and mid-frequency structure: a dominant low-energy peak appears near $\sim 25 - 27$ meV followed by a broad manifold around $\sim 40 - 50$ meV and additional peaks approaching $\sim 55 - 60$ meV. The internal depletion near $\sim 62 - 65$ meV remains a robust feature, and a reduced but still nonzero high-energy tail persists up to ~ 90 meV. Compared with Fig. 5(e), the strongest low-energy accumulation shifts upward (from $\sim 18 - 20$ meV to $\sim 25 - 27$ meV), while the mid-band retains significant intensity, underscoring that partial inversion tunes the balance between low-frequency and mid-frequency vibrational populations.

4 Conclusions

This study delivers a consistent, configuration-aware set of electronic, phonon, and magnon excitation spectra for spinel ferrites spanning magnetite, jacobite, and Mn–Zn mixed ferrites. The workflow com-

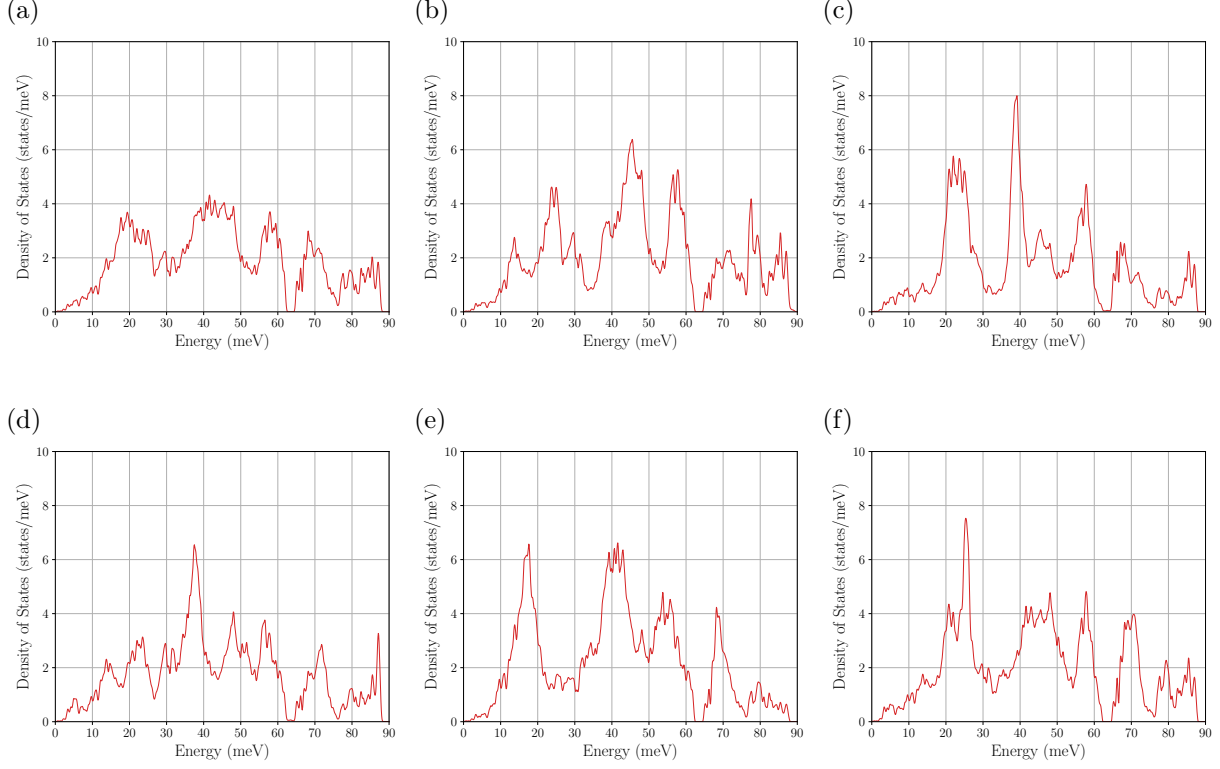


Figure 5: Phonon DOS for spinel ferrites with different cationic compositions and configurations. (a) archetypal Fe_3O_4 , (b) $MnFe_2O_4$ Config. 1 where all Mn atoms occupy A-sites of the spinel structure, (c) $MnFe_2O_4$ Config. 2 where half of the Mn atoms occupy A-sites and the other half occupy B-sites, (d) $(Mn_{0.5}, Zn_{0.5})Fe_2O_4$ Config. 1 where all Zn & Mn atoms occupy A-sites, (e) $(Mn_{0.5}, Zn_{0.5})Fe_2O_4$ Config. 2 where all Zn atoms occupy A-sites & all Mn atoms occupy B-sites, (f) $(Mn_{0.5}, Zn_{0.5})Fe_2O_4$ Config. 3 where all Zn atoms occupy A-sites & the Mn atoms occupy half A-sites and half B-sites.

bines a self-consistent LR determination of Hubbard U and Hund's J parameters within rotationally invariant DFT+ U + J , energy mapping onto a Heisenberg model suitable for mixed-cation sub-lattices, linear spin-wave calculations for magnons, and finite-displacement phonons computed on the same relaxed structures. This alignment across methods ensures that the resulting spectra form a coherent dataset in which differences are attributable to chemistry and A/B-site configurations.

The results underscore that the excitation spectrum is the appropriate microscopic object for comparing ferrites across a composition-configuration landscape. Changes in inversion and site occupation redistribute d - p hybridization and re-weight exchange pathways, thereby shifting electronic, vibrational, and spin-wave spectral features in correlated ways. These configuration-resolved DOS are therefore not merely post-processing outputs; they are compact representations of how local chemistry and lattice topology shape the available excitation channels in each material.

Future work can proceed in two complementary directions. On the materials side, the configurational space can be expanded (e.g., with additional inversion levels and disorder realizations) and the magnetic model refined (further-neighbor exchanges and, where necessary, anisotropy terms) to produce more complete, experimentally comparable spectra. On the modeling side, the computed electron/magnon/phonon DOS provide standardized inputs for frameworks that require microscopic excitation content—particularly those aimed at interpreting or predicting material response under time-dependent fields—so that performance changes can be traced back to identifiable spectral shifts rather than treated as changes in empirical constants. The latter is presented in a forthcoming paper that employs the SEAQT formalism.

Acknowledgments

D.D. would like to acknowledge helpful discussions with Dr. Lórien MacEnulty on linear response calculations and the Department of Materials Science and Engineering for financial support of his doctoral research. The authors thank the Advanced Research Computing (ARC) at Virginia Tech for providing the computational resources and technical support that have contributed to the results reported here.

References

- (1) *Modern Ferrites: Volume 2: Emerging Technologies and Applications*; Harris, V. G., Ed.; IEEE Press, Wiley: Hoboken, NJ, 2023.
- (2) Somiya, S., *Handbook of Advanced Ceramics: Materials, Applications, Processing, and Properties*, 2nd ed; Elsevier Science & Technology: San Diego, 2013.
- (3) Harris, V. G. Modern Microwave Ferrites. *IEEE Transactions on Magnetics* **2012**, *48*, 1075–1104.
- (4) Cullity, B. D.; Graham, C. D., *Introduction to Magnetic Materials*, 1st ed.; Wiley: 2008.
- (5) Smit, J.; Wijn, H. P. J., *Ferrites; Physical Properties of Ferrimagnetic Oxides in Relation to Their Technical Applications. [Translated by G.E. Luton]*; Philips' Technical Library: Eindhoven, 1959.
- (6) Ziese, M.; Höhne, R.; Hong, N.; Dienelt, J.; Zimmer, K.; Esquinazi, P. Magnetoresistance at Grain Boundaries Artificially Introduced into Magnetite Films. *Journal of Magnetism and Magnetic Materials* **2002**, *242*–245, 450–452.
- (7) Cornell, R. M.; Schwertmann, U., *The Iron Oxides: Structure, Properties, Reactions, Occurrences and Uses*, 1st ed.; Wiley: 2003.
- (8) Balaji, G.; Gajbhiye, N.; Wilde, G.; Weissmüller, J. Magnetic Properties of MnFe₂O₄ Nanoparticles. *Journal of Magnetism and Magnetic Materials* **2002**, *242*, 617–620.
- (9) Hakami, O. Structural, Dielectric and Magnetic Properties of MnFe₂O₄/ MWCNTs Based Nanocomposites for Technological Applications. *Surfaces and Interfaces* **2024**, *49*, 104387.
- (10) *High Resistivity High Initial Permeability Mn-Zn Ferrite Applied for 10 MHz Range*; JFE Technical Report 27; JFE Steel Corporation / JFE Ferrite Co., Ltd., 2022.
- (11) He, J.; Yuan, H.; Nie, M.; Guo, H.; Yu, H.; Liu, Z.; Sun, R. Soft Magnetic Materials for Power Inductors: State of Art and Future Development. *Materials Today Electronics* **2023**, *6*, 100066.
- (12) Thakur, P.; Chahar, D.; Taneja, S.; Bhalla, N.; Thakur, A. A Review on MnZn Ferrites: Synthesis, Characterization and Applications. *Ceramics International* **2020**, *46*, 15740–15763.
- (13) Srivastava, A. K.; Hurben, M. J.; Wittenauer, M. A.; Kabos, P.; Patton, C. E.; Ramesh, R.; Dorsey, P. C.; Chrisey, D. B. Angle Dependence of the Ferromagnetic Resonance Linewidth and Two Magnon Losses in Pulsed Laser Deposited Films of Yttrium Iron Garnet, MnZn Ferrite, and NiZn Ferrite. *Journal of Applied Physics* **1999**, *85*, 7838–7848.
- (14) Sun, K.; Lan, Z.; Yu, Z.; Xu, Z.; Jiang, X.; Wang, Z.; Liu, Z.; Luo, M. Temperature and Frequency Characteristics of Low-Loss MnZn Ferrite in a Wide Temperature Range. *Journal of Applied Physics* **2011**, *109*, 106103.
- (15) Beretta, G. P. Steepest Entropy Ascent Model for Far-Nonequilibrium Thermodynamics: Unified Implementation of the Maximum Entropy Production Principle. *Physical Review E* **2014**, *90*, 042113.
- (16) Li, G.; von Spakovsky, M. R. Generalized Thermodynamic Relations for a System Experiencing Heat and Mass Diffusion in the Far-from-Equilibrium Realm Based on Steepest Entropy Ascent. *Physical Review E* **2016**, *94*, 032117.
- (17) Li, G.; von Spakovsky, M. R. Steepest-Entropy-Ascent Quantum Thermodynamic Modeling of the Relaxation Process of Isolated Chemically Reactive Systems Using Density of States and the Concept of Hypoequilibrium State. *Physical Review E* **2016**, *93*, 012137.
- (18) Li, G.; von Spakovsky, M. R. Steepest-Entropy-Ascent Model of Mesoscopic Quantum Systems Far from Equilibrium along with Generalized Thermodynamic Definitions of Measurement and Reservoir. *Physical Review E* **2018**, *98*, 042113.
- (19) Li, G.; von Spakovsky, M. R.; Hin, C. Steepest Entropy Ascent Quantum Thermodynamic Model of Electron and Phonon Transport. *Physical Review B* **2018**, *97*, 024308.

(20) Worden, J. A.; von Spakovsky, M. R.; Hin, C. Predicting Coupled Electron and Phonon Transport Using Steepest-Entropy-Ascent Quantum Thermodynamics, 2024.

(21) Santos-Carballal, D.; Roldan, A.; Grau-Crespo, R.; De Leeuw, N. H. First-Principles Study of the Inversion Thermodynamics and Electronic Structure of Fe M 2 X 4 (Thio)Spinsels (M = Cr , Mn, Co, Ni; X = O , S). *Physical Review B* **2015**, *91*, 195106.

(22) Naveas, N.; Pulido, R.; Marini, C.; Garigiani, P.; Hernandez-Montelongo, J.; Brito, I.; Manso-Silván, M. First-Principles Calculations of Magnetite (Fe_3O_4) above the Verwey Temperature by Using Self-Consistent DFT + U + V . *Journal of Chemical Theory and Computation* **2023**, *19*, 8610–8623.

(23) Sakurai, S.; Sasaki, S.; Okube, M.; Ohara, H.; Toyoda, T. Cation Distribution and Valence State in Mn–Zn Ferrite Examined by Synchrotron X-rays. *Physica B: Condensed Matter* **2008**, *403*, 3589–3595.

(24) Becke, A. D. Perspective: Fifty Years of Density-Functional Theory in Chemical Physics. *The Journal of Chemical Physics* **2014**, *140*, 18A301.

(25) Meng, Y.; Liu, X.-W.; Huo, C.-F.; Guo, W.-P.; Cao, D.-B.; Peng, Q.; Dearden, A.; Gonze, X.; Yang, Y.; Wang, J.; Jiao, H.; Li, Y.; Wen, X.-D. When Density Functional Approximations Meet Iron Oxides. *Journal of Chemical Theory and Computation* **2016**, *12*, 5132–5144.

(26) *Correlated Electrons: From Models to Materials: Lecture Notes of the Autumn School Correlated Electrons 2012: At Forschungszentrum Jülich, 3-7 September 2012*; Pavarini, E., Koch, E., Anders, F., Jarrell, M., Institute for Advanced Simulation, German Research School for Simulation Sciences, Eds.; Schriften Des Forschungszentrums Jülich. Reihe Modeling and Simulation Band 2; Forschungszentrum Jülich, Zentralbibliothek, Verl: Jülich, 2012.

(27) Anisimov, V. I.; Aryasetiawan, F.; Lichtenstein, A. I. First-Principles Calculations of the Electronic Structure and Spectra of Strongly Correlated Systems: The LDA + U Method. *Journal of Physics: Condensed Matter* **1997**, *9*, 767–808.

(28) Bajaj, A.; Kulik, H. J. Molecular DFT+U: A Transferable, Low-Cost Approach to Eliminate Delocalization Error. *The Journal of Physical Chemistry Letters* **2021**, *12*, 3633–3640.

(29) Linscott, E. B.; Cole, D. J.; Payne, M. C.; O'Regan, D. D. Role of Spin in the Calculation of Hubbard U and Hund's J Parameters from First Principles. *Physical Review B* **2018**, *98*, 235157.

(30) Streletsov, S. V.; Khomskii, D. I. Orbital Physics in Transition Metal Compounds: New Trends. *Physics-Uspekhi* **2017**, *60*, 1121–1146.

(31) Georges, A.; Medici, L. D.; Mravlje, J. Strong Correlations from Hund's Coupling. *Annual Review of Condensed Matter Physics* **2013**, *4*, 137–178.

(32) Dudarev, S. L.; Botton, G. A.; Savrasov, S. Y.; Humphreys, C. J.; Sutton, A. P. Electron-Energy-Loss Spectra and the Structural Stability of Nickel Oxide: An LSDA+U Study. *Physical Review B* **1998**, *57*, 1505–1509.

(33) Leiria Campo Jr, V.; Cococcioni, M. Extended DFT + U + V Method with On-Site and Inter-Site Electronic Interactions. *Journal of Physics: Condensed Matter* **2010**, *22*, 055602.

(34) Wang, Y.-C.; Chen, Z.-H.; Jiang, H. The Local Projection in the Density Functional Theory plus U Approach: A Critical Assessment. *The Journal of Chemical Physics* **2016**, *144*, 144106.

(35) Moore, G. C.; Horton, M. K.; Linscott, E.; Ganose, A. M.; Siron, M.; O'Regan, D. D.; Persson, K. A. High-Throughput Determination of Hubbard U and Hund J Values for Transition Metal Oxides via the Linear Response Formalism. *Physical Review Materials* **2024**, *8*, 014409.

(36) Cococcioni, M.; De Gironcoli, S. Linear Response Approach to the Calculation of the Effective Interaction Parameters in the LDA + U Method. *Physical Review B* **2005**, *71*, 035105.

(37) Vaugier, L.; Jiang, H.; Biermann, S. Hubbard U and Hund Exchange J in Transition Metal Oxides: Screening versus Localization Trends from Constrained Random Phase Approximation. *Physical Review B* **2012**, *86*, 165105.

(38) Kresse, G.; Hafner, J. *Ab Initio* Molecular Dynamics for Liquid Metals. *Physical Review B* **1993**, *47*, 558–561.

(39) Kresse, G.; Furthmüller, J.; Hafner, J. Theory of the Crystal Structures of Selenium and Tellurium: The Effect of Generalized-Gradient Corrections to the Local-Density Approximation. *Physical Review B* **1994**, *50*, 13181–13185.

(40) Kresse, G.; Furthmüller, J. Efficiency of Ab-Initio Total Energy Calculations for Metals and Semiconductors Using a Plane-Wave Basis Set. *Computational Materials Science* **1996**, *6*, 15–50.

(41) Kresse, G.; Furthmüller, J. Efficient Iterative Schemes for *Ab Initio* Total-Energy Calculations Using a Plane-Wave Basis Set. *Physical Review B* **1996**, *54*, 11169–11186.

(42) Kresse, G.; Joubert, D. From Ultrasoft Pseudopotentials to the Projector Augmented-Wave Method. *Physical Review B* **1999**, *59*, 1758–1775.

(43) Perdew, J. P.; Burke, K.; Ernzerhof, M. Generalized Gradient Approximation Made Simple. *Physical Review Letters* **1996**, *77*, 3865–3868.

(44) Monkhorst, H. J.; Pack, J. D. Special Points for Brillouin-zone Integrations. *Physical Review B* **1976**, *13*, 5188–5192.

(45) Bader, R. F. W., *Atoms in Molecules: A Quantum Theory*; The International Series of Monographs on Chemistry 22; Clarendon Press ; Oxford University Press: Oxford [England] : New York, 1994.

(46) Henkelman, G.; Arnaldsson, A.; Jónsson, H. A Fast and Robust Algorithm for Bader Decomposition of Charge Density. *Computational Materials Science* **2006**, *36*, 354–360.

(47) Tang, W.; Sanville, E.; Henkelman, G. A Grid-Based Bader Analysis Algorithm without Lattice Bias. *Journal of Physics: Condensed Matter* **2009**, *21*, 084204.

(48) Yu, M.; Trinkle, D. R. Accurate and Efficient Algorithm for Bader Charge Integration. *The Journal of Chemical Physics* **2011**, *134*, 064111.

(49) Liechtenstein, A. I.; Anisimov, V. I.; Zaanen, J. Density-Functional Theory and Strong Interactions: Orbital Ordering in Mott-Hubbard Insulators. *Physical Review B* **1995**, *52*, R5467–R5470.

(50) Hımmetoglu, B.; Floris, A.; De Gironcoli, S.; Cococcioni, M. Hubbard-Corrected DFT Energy Functionals: The LDA+U Description of Correlated Systems. *International Journal of Quantum Chemistry* **2014**, *114*, 14–49.

(51) Lambert, D. S.; O'Regan, D. D. Evaluation of First-Principles Hubbard and Hund Corrected DFT for Defect Formation Energies in Non-Magnetic Transition Metal Oxides. *RSC Advances* **2024**, *14*, 38645–38659.

(52) MacEnulty, L.; O'Regan, D. D. Optimization Strategies Developed on NiO for Heisenberg Exchange Coupling Calculations Using Projector Augmented Wave Based First-Principles DFT+U+J. *Physical Review B* **2023**, *108*, 245137.

(53) Heisenberg, W. Zur Theorie des Ferromagnetismus. *Zeitschrift für Physik* **1928**, *49*, 619–636.

(54) Singh, N. The Story of Magnetism: From Heisenberg, Slater, and Stoner to Van Vleck, and the Issues of Exchange and Correlation, 2018.

(55) Liechtenstein, A.; Katsnelson, M.; Antropov, V.; Gubanov, V. Local Spin Density Functional Approach to the Theory of Exchange Interactions in Ferromagnetic Metals and Alloys. *Journal of Magnetism and Magnetic Materials* **1987**, *67*, 65–74.

(56) Katsnelson, M. I.; Lichtenstein, A. I. First-Principles Calculations of Magnetic Interactions in Correlated Systems. *Physical Review B* **2000**, *61*, 8906–8912.

(57) Xiang, H.; Lee, C.; Koo, H.-J.; Gong, X.; Whangbo, M.-H. Magnetic Properties and Energy-Mapping Analysis. *Dalton Trans.* **2013**, *42*, 823–853.

(58) Harris, V. G.; Andalib, P. In *Modern Ferrites*, Harris, V. G., Ed., 1st ed.; Wiley: 2022, pp 31–67.

(59) Srivastava, C. M.; Srinivasan, G.; Nanadikar, N. G. Exchange Constants in Spinel Ferrites. *Physical Review B* **1979**, *19*, 499–508.

(60) Glasser, M. L.; Milford, F. J. Spin wave spectra of magnetite. *Physical Review* **1963**, *130*, 1783.

(61) Bercoff, P.; Bertorello, H. Exchange Constants and Transfer Integrals of Spinel Ferrites. *Journal of Magnetism and Magnetic Materials* **1997**, *169*, 314–322.

(62) Ciofini, I.; Adamo, C.; Barone, V.; Berthier, G.; Rassat, A. Mapping the Many-Electron Generalised Spin-Exchange Hamiltonian to Accurate Post-HF Calculations. *Chemical Physics* **2005**, *309*, 133–141.

(63) Holstein, T.; Primakoff, H. Field Dependence of the Intrinsic Domain Magnetization of a Ferromagnet. *Physical Review* **1940**, *58*, 1098–1113.

(64) Auerbach, A., *Interacting Electrons and Quantum Magnetism*; Birman, J. L., Lynn, J. W., Silverman, M. P., Stanley, H. E., Voloshin, M., Eds.; Graduate Texts in Contemporary Physics; Springer New York: New York, NY, 1994.

(65) Toth, S.; Lake, B. Linear Spin Wave Theory for Single-Q Incommensurate Magnetic Structures. *Journal of Physics: Condensed Matter* **2015**, *27*, 166002.

(66) Colpa, J. Diagonalization of the Quadratic Boson Hamiltonian. *Physica A: Statistical Mechanics and its Applications* **1978**, *93*, 327–353.

(67) Camley, R. E.; Livesey, K. L. Consequences of the Dzyaloshinskii-Moriya Interaction. *Surface Science Reports* **2023**, *78*, 100605.

(68) McQueeney, R. J.; Yethiraj, M.; Montfrooij, W.; Gardner, J. S.; Metcalf, P.; Honig, J. M. Investigation of the Presence of Charge Order in Magnetite by Measurement of the Spin Wave Spectrum. *Physical Review B* **2006**, *73*, 174409.

(69) Togo, A.; Oba, F.; Tanaka, I. First-Principles Calculations of the Ferroelastic Transition between Rutile-Type and CaCl₂-Type SiO₂ at High Pressures. *Physical Review B* **2008**, *78*, 134106.

(70) Togo, A.; Tanaka, I. First Principles Phonon Calculations in Materials Science. *Scripta Materialia* **2015**, *108*, 1–5.

(71) Parlinski, K.; Li, Z. Q.; Kawazoe, Y. First-Principles Determination of the Soft Mode in Cubic ZrO₂. *Physical Review Letters* **1997**, *78*, 4063–4066.

(72) Bohra, M.; Alman, V.; Arras, R. Nanostructured ZnFe₂O₄: An Exotic Energy Material. *Nanomaterials* **2021**, *11*, 1286.

(73) Bock, D. C. et al. (De)Lithiation of Spinel Ferrites Fe₃O₄, MgFe₂O₄, and ZnFe₂O₄: A Combined Spectroscopic, Diffraction and Theory Study. *Physical Chemistry Chemical Physics* **2020**, *22*, 26200–26215.

(74) Anantharaman, M.; Jagatheesan, S.; Malini, K.; Sindhu, S.; Narayanasamy, A.; Chinanasamy, C.; Jacobs, J.; Reijne, S.; Seshan, K.; Smits, R.; Brongersma, H. On the Magnetic Properties of Ultra-Fine Zinc Ferrites. *Journal of Magnetism and Magnetic Materials* **1998**, *189*, 83–88.

(75) Rodríguez Torres, C. E.; Golmar, F.; Ziese, M.; Esquinazi, P.; Heluani, S. P. Evidence of Defect-Induced Ferromagnetism in ZnFe₂O₄ Thin Films. *Physical Review B* **2011**, *84*, 064404.

(76) Chai, Z.; Si, R.; Chen, M.; Teobaldi, G.; O'Regan, D. D.; Liu, L.-M. Minimum Tracking Linear Response Hubbard and Hund Corrected Density Functional Theory in CP2K. *Journal of Chemical Theory and Computation* **2024**, *20*, 8984–9002.

(77) Gebauer, R. Oxygen Vacancies in Zirconia and Their Migration: The Role of Hubbard-U Parameters in Density Functional Theory. *Crystals* **2023**, *13*, 574.

(78) Sala, G. et al. Van Hove Singularity in the Magnon Spectrum of the Antiferromagnetic Quantum Honeycomb Lattice. *Nature Communications* **2021**, *12*, 171.

(79) Van Hove, L. The Occurrence of Singularities in the Elastic Frequency Distribution of a Crystal. *Physical Review* **1953**, *89*, 1189–1193.